Sciencexpress Reports

Single-proton spin detection by diamond magnetometry

M. Loretz,[1] T. Rosskopf,[1] J. M. Boss,[1] S. Pezzagna,[2] J. Meijer,[2] C. L. Degen[1]*

[1]Department of Physics, ETH Zurich, Otto Stern Weg 1, 8093 Zurich, Switzerland.

[2]Institute for Experimental Physics II, Department of Nuclear Solid State Physics, Universität Leipzig, Linnéstrasse 5, D-04103 Leipzig, Germany.

*Corresponding author. E-mail: degenc@ethz.ch

Extending magnetic resonance imaging to the atomic scale has been a long-standing aspiration, driven by the prospect of directly mapping atomic positions in molecules with three-dimensional spatial resolution. We report detection of individual, isolated proton spins by a nitrogen-vacancy (NV) center in a diamond chip covered by an inorganic salt. The single-proton identity was confirmed by the Zeeman effect and by a quantum coherent rotation of the weakly coupled nuclear spin. Using the hyperfine field of the NV center as an imaging gradient, we determined proton-NV distances of less than 1 nm.

Magnetic resonance imaging (MRI) is well known from clinical medicine for providing noninvasive images of objects with three-dimensional resolution and rich image contrast. Although MRI is typically limited to micrometer-to-millimeter-sized samples (*1*), extension to voxels of a few $(\text{nm})^3$ containing 10^2–10^6 nuclear spins has recently been reported by several techniques, including magnetic resonance force microscopy (*2*, *3*) and diamond-based magnetometry (*4*–*7*). The ultimate goal of such nano-MRI is the direct mapping of atomic coordinates with single spin sensitivity (*8*, *9*). This capability is expected to greatly aid structure determination of proteins and other complex biological molecules and would be extremely useful for the chemical analysis of nanostructured surfaces and associated dynamics.

We present a step toward such an atomic-resolution MRI technique by detecting the nuclear magnetic resonance (NMR) signal from isolated hydrogen nuclei formed at the surface of a diamond chip. Our measurements take advantage of near-surface nitrogen-vacancy centers (NV centers) that could be coherently coupled to the weakly interacting nuclear spins. By utilizing the hyperfine field of the NV center as an imaging gradient, we could further determine the relative location of the hydrogen nuclei, providing a simple form of two-dimensional MRI with atomic resolution. The results suggest that diamond-based NMR sensors provide a viable route toward the three-dimensional spatial mapping of atoms in molecules.

The NV center is a prototype single spin system that can be optically initialized and read out at room temperature (*10*). The electronic spin has a long coherence time that has proven especially useful for quantum information processing and high-resolution magnetic sensing applications (*11*–*14*). Diamond magnetometry has recently enabled important advances toward nanoscale NMR detection, including the identification of up to 8 ^{13}C nuclei within the diamond lattice (*15*–*18*), the detection of small ensembles of ^{1}H, ^{19}F, ^{29}Si, and ^{31}P nuclei applied to a diamond chip (*4*–*6*, *7*, *19*), and scanning probe imaging with a resolution approaching 10 nm (*20*, *21*).

Of central importance to sensitive NMR measurements are NV centers positioned near the diamond surface that maintain their negative charge state and a long spin coherence time. In our study, NV centers were created at ~10 nm depth in a commercial (001) single crystal diamond substrate by low-energy ion implantation (*22*), followed by a slow removal of the top diamond layers by oxidative etching until the depth was <3 nm (*6*). Even at this close proximity, the NV spins had long coherence times of up to 200 μs under dynamical decoupling. To introduce the proton spins, the diamond chip was coated with a thin film of ammonium hexafluorophosphate (NH_4PF_6) by thermal evaporation. We found that the combination of oxidative etching and NH_4PF_6 deposition introduced a slight, atomic-scale topography to the surface (~1 nm-rms) that resulted in the formation of isolated hydrogen nuclei (Fig. 1A).

The experimental setup was a home-built confocal microscope that operated under ambient conditions and used 532-nm laser light together with a single photon counter to polarize and detect the NV center. The microscope was equipped with a coplanar waveguide to apply microwave pulses to the electronic spin. A moveable permanent magnet provided a static field of $B_0 \sim 180$ mT. NMR signals were detected using a multi-pulse detection sequence based on Carr-Purcell decoupling (Fig. 1B) whose detection frequency could be tuned in and out of resonance with the nuclear Larmor precession by adjusting the interpulse delay (*5*, *6*, *23*, *24*). At resonance with a specific nuclear spin species, the nuclear magnetic noise accelerates the decoherence of the NV center, reflected in an enhanced rate of transitions between spin states. The reported signals present the probability P (with values between 0 and 1) of a spin transition occurring between the NV center's $m_S = 0$ and $m_S = -1$ spin states during a chosen evolution time T.

Figure 1C shows typical NMR spectra recorded by 5 different NV centers. We found all spectra to show a peak in the transition probability at the expected ^{1}H NMR frequency given by $\gamma_n B_0$, where $\gamma_n/2\pi = 42.57$ MHz/T is the proton gyromagnetic ratio. This "bath peak" originates from an ensemble of more distant protons, such as those in terminating surface groups, surface-adsorbed molecules or NH_4PF_6 (*6*, *20*, *21*). By contrast, the most striking features in the spectra were strong additional resonances that appeared at slightly higher frequencies than the expected ^{1}H position.

The peak frequencies depended on the magnitude of the applied static field B_0 with a linear slope given by γ_n (Fig. 2, A and B). This identifies all peaks as proton resonances. Moreover, we found that the frequency differences between peaks were independent of B_0 to within experimental error (Fig. 2C). Such behavior is expected for nuclear spins that experience a hyperfine interaction; in the limit of strong external field $B_0 >> a_\parallel/\gamma_n$, the frequency offset then represents one-half the parallel component $a_\parallel$ of the hyperfine coupling tensor (*15*, *17*, *25*). The observations in Fig. 2 are strong evidence that all resonances are related to ^{1}H nuclei, and not for example to the NV center's ^{15}N nucleus or imperfections of the multipulse detection sequence. No extra ^{1}H peaks were seen with other surface coatings on at least 20 NV centers. Additional data and control measurements are given in the supplementary materials (*25*).

We verified that resonances originated from single nuclei by exploiting the quantum nature of sensor and target spins. Figure 3 displays the transition probability for the peak (red rectangle) of NV4 (Fig. 1C) for a progressively longer evolution time T. The transition probability showed an oscillatory behavior that signals a coherent joint rotation entangling the electronic and nuclear spins (*15*). In particular, the transition probability well exceeded the $P = 0.5$ threshold that distinguishes quantum coupling from classical decoherence (*16*). The oscillation could be well

Downloaded from www.sciencemag.org on October 29, 2014

reproduced by a density operator calculation (shown with Fig. 3) that took the Zeeman and hyperfine interactions of the single nuclear spin into account (*25*). Although quantum coherent coupling could also result from small proton clusters, we found that only single protons can generate the oscillation observed in Fig. 3. The additional resonance in the spectrum therefore must result from a solitary hydrogen nucleus, and cannot for example be caused by a H_2 molecule, $–CH_2/–CH_3$ group, or NH_4^+ ion. From the oscillation period we could further directly deduce the transverse component of the hyperfine coupling tensor as $a_\perp/2\pi$ = 14.5 ± 0.3 kHz (*25*).

Assuming that the hyperfine interaction is dipolar, we can use the values of $a_\parallel$ and $a_\perp$ to infer two out of three spatial coordinates of the protons, thereby realizing a crude form of magnetic resonance imaging with atomic resolution (Fig. 4). Specifically, $a_\parallel = \frac{\mu_0}{4\pi}\gamma_e\gamma_n\hbar r^{-3}\left(3\cos^2\theta - 1\right)$ and $a_\perp = \frac{\mu_0}{4\pi}\gamma_e\gamma_n\hbar r^{-3}3\sin\theta\cos\theta$, where r is distance, θ the interspin angle, $\gamma_e/2\pi$ = 28.02 GHz/T the NV electron gyromagnetic ratio, μ_0 the permeability of free space, and $\hbar$ Planck's constant (*16*, *17*, *25*).

Figure 4 shows that all identified single protons were located very close, less than 1 nm, from the NV center and that positions near the NV symmetry axis (the [111] crystal axis) were favored. Both observations are unexpected. Since the protons were spatially isolated, we speculate that they became bound in troughs of the surface topography and were thus spatially offset from surface adsorbates. Protons may also have become incorporated into the diamond lattice during thermal evaporation or by proton diffusion, although both processes are unlikely (*25*). The favored axial position can be explained in several ways; for example, the axial position may be the only stable configuration for negatively charged NV centers with such nearby hydrogen atoms, as expected from electron density calculations (*26*), or local effects like paramagnetic surface defects could shift the nuclear spin levels and enhance $a_\parallel$ (*27*).

The detection of single ^{1}H nuclei presents an important step toward diamond-based nano-MRI. Although in our study the placement of protons was stochastic and did not reflect the original structure of the applied sample, the technique provides many opportunities for future imaging experiments. In order to resolve neighboring nuclei in larger molecules with many atoms, for example, one may consider introducing a nanoscale magnetic gradient, such as the high gradients provided by scannable magnetic tips (*28*, *29*) or current-carrying constrictions (*3*). Alternatively, one could improve the spectral resolution using correlation measurements (*30*, *31*) or by analyzing internuclear couplings, like spin pairs (*32*). By introducing nuclear or electronic spin labels—a routine technique in protein NMR—one could finally target specific sites in a molecule.

Ultimately, the molecular imaging capability will be bounded by detection sensitivity, which sets a limit on the maximum distance at which a single proton can be sensed. This constrains the size of a target molecule. For our experiments, detection sensitivity was limited by photon shot noise to about 23 nT when allowing for one minute of averaging. This corresponds to a proton hyperfine field at a separation of approximately $r \approx 4$ nm (*25*). Recent advances to NV signal detection could enhance this sensitivity by at least one order of magnitude, including efficient microfabricated photon collectors (*33*, *34*), quantum storage and error correction protocols (*35*, *36*), hyperpolarization (*37*), and mediating electron spins (*38*, *39*). Assuming the atomic sensitivity can be extended to a sensor stand-off of 10 nm, diamond-based nano-MRI could contribute detailed structural information on many important systems in the nanosciences, such as proteins in biological membranes or polymer assemblies in patterned media.

References and Notes

1. P. Glover, P. Mansfield, Limits to magnetic resonance microscopy. *Rep. Prog. Phys.* **65**, 1489–1511 (2002). doi:10.1088/0034-4885/65/10/203
2. C. L. Degen, M. Poggio, H. J. Mamin, C. T. Rettner, D. Rugar, Nanoscale magnetic resonance imaging. *Proc. Natl. Acad. Sci. U.S.A.* **106**, 1313–1317 (2009). Medline doi:10.1073/pnas.0812068106
3. J. M. Nichol, T. R. Naibert, E. R. Hemesath, L. J. Lauhon, R. Budakian, Nanoscale Fourier-transform magnetic resonance imaging. *Phys. Rev. X* **3**, 031016 (2013) . doi:10.1103/PhysRevX.3.031016
4. H. J. Mamin, M. Kim, M. H. Sherwood, C. T. Rettner, K. Ohno, D. D. Awschalom, D. Rugar, Nanoscale nuclear magnetic resonance with a nitrogen-vacancy spin sensor. *Science* **339**, 557–560 (2013). Medline doi:10.1126/science.1231540
5. T. Staudacher, F. Shi, S. Pezzagna, J. Meijer, J. Du, C. A. Meriles, F. Reinhard, J. Wrachtrup, Nuclear magnetic resonance spectroscopy on a (5-nanometer)^3 sample volume. *Science* **339**, 561–563 (2013). Medline doi:10.1126/science.1231675
6. M. Loretz, S. Pezzagna, J. Meijer, C. L. Degen, Nanoscale nuclear magnetic resonance with a 1.9-nm-deep nitrogen-vacancy sensor. *Appl. Phys. Lett.* **104**, 033102 (2014). doi:10.1063/1.4862749
7. C. Müller, X. Kong, J. M. Cai, K. Melentijević, A. Stacey, M. Markham, D. Twitchen, J. Isoya, S. Pezzagna, J. Meijer, J. F. Du, M. B. Plenio, B. Naydenov, L. P. McGuinness, F. Jelezko, Nuclear magnetic resonance spectroscopy with single spin sensitivity. *Nat. Commun.* **5**, 4703–4703 (2014). Medline doi:10.1038/ncomms5703
8. J. A. Sidles, Noninductive detection of single-proton magnetic resonance. *Appl. Phys. Lett.* **58**, 2854 (1991). doi:10.1063/1.104757
9. C. L. Degen, Scanning magnetic field microscope with a diamond single-spin sensor. *Appl. Phys. Lett.* **92**, 243111 (2008). doi:10.1063/1.2943282
10. A. Gruber, A. Drabenstedt, C. Tietz, L. Fleury, J. Wrachtrup, C. von Borczyskowski, Scanning confocal optical microscopy and magnetic resonance on single defect centers. *Science* **276**, 2012–2014 (1997). doi:10.1126/science.276.5321.2012
11. R. Hanson, V. V. Dobrovitski, A. E. Feiguin, O. Gywat, D. D. Awschalom, Coherent dynamics of a single spin interacting with an adjustable spin bath. *Science* **320**, 352–355 (2008). Medline doi:10.1126/science.1155400
12. P. C. Maurer, G. Kucsko, C. Latta, L. Jiang, N. Y. Yao, S. D. Bennett, F. Pastawski, D. Hunger, N. Chisholm, M. Markham, D. J. Twitchen, J. I. Cirac, M. D. Lukin, Room-temperature quantum bit memory exceeding one second. *Science* **336**, 1283–1286 (2012). Medline doi:10.1126/science.1220513
13. M. S. Grinolds, S. Hong, P. Maletinsky, L. Luan, M. D. Lukin, R. L. Walsworth, A. Yacoby, Nanoscale magnetic imaging of a single electron spin under ambient conditions. *Nat. Phys.* **9**, 215–219 (2013). doi:10.1038/nphys2543
14. J. P. Tetienne, T. Hingant, J. V. Kim, L. H. Diez, J. P. Adam, K. Garcia, J. F. Roch, S. Rohart, A. Thiaville, D. Ravelosona, V. Jacques, Nanoscale imaging and control of domain-wall hopping with a nitrogen-vacancy center microscope. *Science* **344**, 1366–1369 (2014). Medline doi:10.1126/science.1250113
15. T. H. Taminiau, J. J. T. Wagenaar, T. van der Sar, F. Jelezko, V. V. Dobrovitski, R. Hanson, Detection and control of individual nuclear spins using a weakly coupled electron spin. *Phys. Rev. Lett.* **109**, 137602 (2012). Medline doi:10.1103/PhysRevLett.109.137602
16. N. Zhao, J. Honert, B. Schmid, M. Klas, J. Isoya, M. Markham, D. Twitchen, F. Jelezko, R. B. Liu, H. Fedder, J. Wrachtrup, Sensing single remote nuclear spins. *Nat. Nanotechnol.* **7**, 657–662 (2012). Medline doi:10.1038/nnano.2012.152
17. S. Kolkowitz, Q. P. Unterreithmeier, S. D. Bennett, M. D. Lukin, Sensing distant nuclear spins with a single electron spin. *Phys. Rev. Lett.* **109**, 137601 (2012). Medline doi:10.1103/PhysRevLett.109.137601
18. R. Schirhagl, K. Chang, M. Loretz, C. L. Degen, Nitrogen-vacancy centers in diamond: Nanoscale sensors for physics and biology. *Annu. Rev. Phys. Chem.* **65**, 83–105 (2014). Medline doi:10.1146/annurev-physchem-040513-103659
19. S. DeVience, L. M. Pham, I. Lovchinsky, A. O. Sushkov, N. Bar-Gill, C. Belthangady, F. Casola, M. Corbett, H. Zhang, M. Lukin, H. Park, A. Yacoby, R. L. Walsworth, Nanoscale NMR spectroscopy and imaging of multiple nuclear species. arXiv:1406.3365 (2014).
20. D. Rugar, H. J. Mamin, M. H. Sherwood, M. Kim, C. T. Rettner, K. Ohno, D. D. Awschalom, Proton magnetic resonance imaging with a nitrogen-vacancy spin sensor. arXiv:1406.2983 (2014).
21. T. Haberle, D. Schmid-Lorch, F. Reinhard, J. Wrachtrup, Scanning probe

microscopy with chemical contrast by nanoscale nuclear magnetic resonance. arXiv:1406.3324 (2014).
22. B. K. Ofori-Okai, S. Pezzagna, K. Chang, M. Loretz, R. Schirhagl, Y. Tao, B. A. Moores, K. Groot-Berning, J. Meijer, C. L. Degen, Spin properties of very shallow nitrogen vacancy defects in diamond. *Phys. Rev. B* **86**, 081406 (2012). doi:10.1103/PhysRevB.86.081406
23. T. Gullion, D. B. Baker, M. S. Conradi, New, compensated Carr-Purcell sequences. *J. Magn. Reson.* **89**, 479–484 (1990).
24. G. de Lange, D. Ristè, V. V. Dobrovitski, R. Hanson, Single-spin magnetometry with multipulse sensing sequences. *Phys. Rev. Lett.* **106**, 080802 (2011). Medline doi:10.1103/PhysRevLett.106.080802
25. Materials and methods are available as supplementary materials at *Science* Online.
26. A. Gali, M. Fyta, E. Kaxiras, Ab initio supercell calculations on nitrogen-vacancy center in diamond: Electronic structure and hyperfine tensors. *Phys. Rev. B* **77**, 155206 (2008). doi:10.1103/PhysRevB.77.155206
27. B. Smeltzer, L. Childress, A. Gali, ^{13}C hyperfine interactions in the nitrogen-vacancy centre in diamond. *New J. Phys.* **13**, 025021 (2011). doi:10.1088/1367-2630/13/2/025021
28. H. J. Mamin, C. T. Rettner, M. H. Sherwood, L. Gao, D. Rugar, High field-gradient dysprosium tips for magnetic resonance force microscopy. *Appl. Phys. Lett.* **100**, 013102 (2012). doi:10.1063/1.3673910
29. M. S. Grinolds, M. Warner, K. De Greve, Y. Dovzhenko, L. Thiel, R. L. Walsworth, S. Hong, P. Maletinsky, A. Yacoby, Subnanometre resolution in three-dimensional magnetic resonance imaging of individual dark spins. *Nat. Nanotechnol.* **9**, 279–284 (2014). Medline doi:10.1038/nnano.2014.30
30. G. M. Leskowitz, Force-detected nuclear magnetic resonance independent of field gradients. Thesis, California Institute of Technology, 2003.
31. A. Laraoui, F. Dolde, C. Burk, F. Reinhard, J. Wrachtrup, C. A. Meriles, High-resolution correlation spectroscopy of ^{13}C spins near a nitrogen-vacancy centre in diamond. *Nat. Commun.* **4**, 1651 (2013). Medline doi:10.1038/ncomms2685
32. F. Shi, X. Kong, P. Wang, F. Kong, N. Zhao, R.-B. Liu, J. Du, Sensing and atomic-scale structure analysis of single nuclear-spin clusters in diamond. *Nat. Phys.* **10**, 21–25 (2014). doi:10.1038/nphys2814
33. J. P. Hadden, J. P. Harrison, A. C. Stanley-Clarke, L. Marseglia, Y.-L. D. Ho, B. R. Patton, J. L. O'Brien, J. G. Rarity, Strongly enhanced photon collection from diamond defect centers under microfabricated integrated solid immersion lenses. *Appl. Phys. Lett.* **97**, 241901 (2010). doi:10.1063/1.3519847
34. T. M. Babinec, B. J. Hausmann, M. Khan, Y. Zhang, J. R. Maze, P. R. Hemmer, M. Loncar, A diamond nanowire single-photon source. *Nat. Nanotechnol.* **5**, 195–199 (2010). Medline doi:10.1038/nnano.2010.6
35. L. Jiang, J. S. Hodges, J. R. Maze, P. Maurer, J. M. Taylor, D. G. Cory, P. R. Hemmer, R. L. Walsworth, A. Yacoby, A. S. Zibrov, M. D. Lukin, Repetitive readout of a single electronic spin via quantum logic with nuclear spin ancillae. *Science* **326**, 267–272 (2009). Medline doi:10.1126/science.1176496
36. T. H. Taminiau, J. Cramer, T. van der Sar, V. V. Dobrovitski, R. Hanson, Universal control and error correction in multi-qubit spin registers in diamond. *Nat. Nanotechnol.* **9**, 171–176 (2014). Medline doi:10.1038/nnano.2014.2
37. P. London, J. Scheuer, J. M. Cai, I. Schwarz, A. Retzker, M. B. Plenio, M. Katagiri, T. Teraji, S. Koizumi, J. Isoya, R. Fischer, L. P. McGuinness, B. Naydenov, F. Jelezko, Detecting and polarizing nuclear spins with double resonance on a single electron spin. *Phys. Rev. Lett.* **111**, 067601 (2013). Medline doi:10.1103/PhysRevLett.111.067601
38. M. Schaffry, E. M. Gauger, J. J. L. Morton, S. C. Benjamin, Proposed spin amplification for magnetic sensors employing crystal defects. *Phys. Rev. Lett.* **107**, 207210 (2011). Medline doi:10.1103/PhysRevLett.107.207210
39. M. D. Lukin, presented at the QuASAR fields meeting (Broomfield CO, USA, 12 September 2014).
40. M. Loretz, T. Rosskopf, C. L. Degen, Radio-frequency magnetometry using a single electron spin. *Phys. Rev. Lett.* **110**, 017602 (2013). Medline doi:10.1103/PhysRevLett.110.017602

Acknowledgments
We thank K. Chang, A. Dussaux, T. Mathis, T. Morf, and R. Schirhagl for experimental support; R. Hanson, F. Jelezko, and C. Ryan for helpful discussions and critical comments; and B. Moores for proofreading the manuscript. This work was supported by the Swiss National Science Foundation through project grant no. 200021_137520/1 and through the NCCR QSIT, and by the FP7-611143 DIADEMS program of the European Commission.

Supplementary Materials
www.sciencemag.org/cgi/content/full/science.1259464/DC1
Materials and Methods
Supplementary Text
Figs. S1 to S5
Tables S1 to S3
References (*40*)

31 July 2014; accepted 7 October 2014
Published online 16 October 2014
10.1126/science.1259464

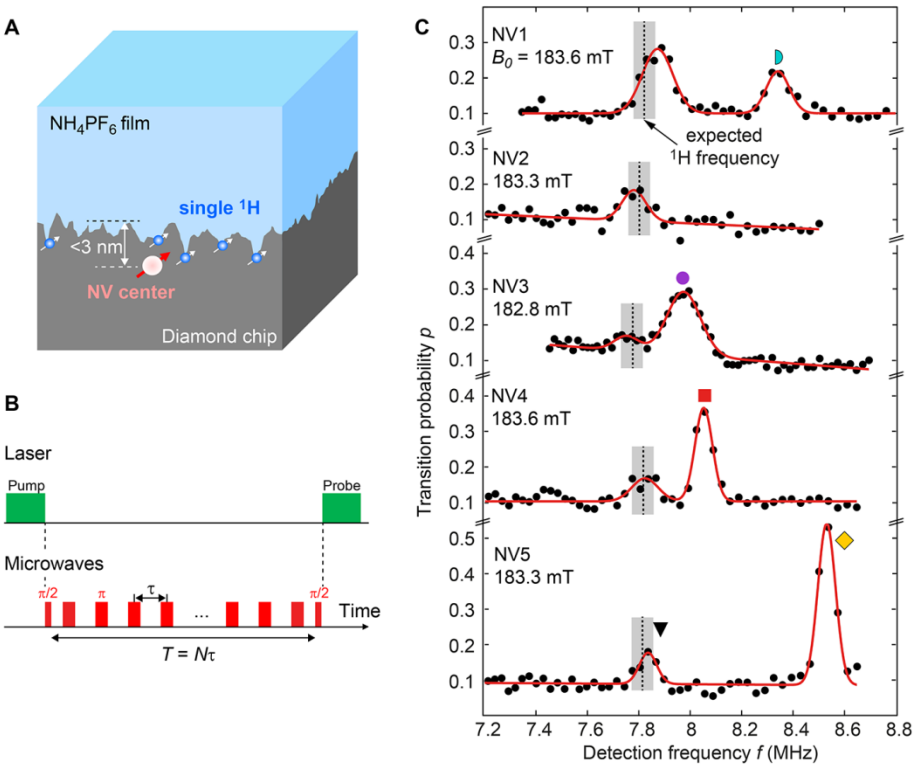

Fig. 1. Basic configuration for single-proton NMR detection. (**A**) Sketch of the diamond sensor chip with NV center, interface region with single protons, and NH_4PF_6 sample. (**B**) Multipulse detection sequence based on Carr-Purcell decoupling. Optical pulses were used to pump and probe the NV spin state via the spin-dependent fluorescence. The detection frequency $f = 1/(2\tau)$ was adjusted by varying the interpulse spacing τ, and N was typically a few hundred. The detection sequence was repeated several million times to build up sufficient photon counting statistics. (**C**) Representative NMR spectra recorded by 5 different NV centers. Plotted is the transition probability between $m_S = 0$ and $m_S = -1$ spin states for a fixed number of pulses N. Black dots are the data and red curves are Gaussian fits. The vertical dashed lines indicate the expected ^{1}H NMR frequencies at the given applied field B_0, and the gray shaded areas reflect the calibration uncertainty (±1 mT) in B_0.

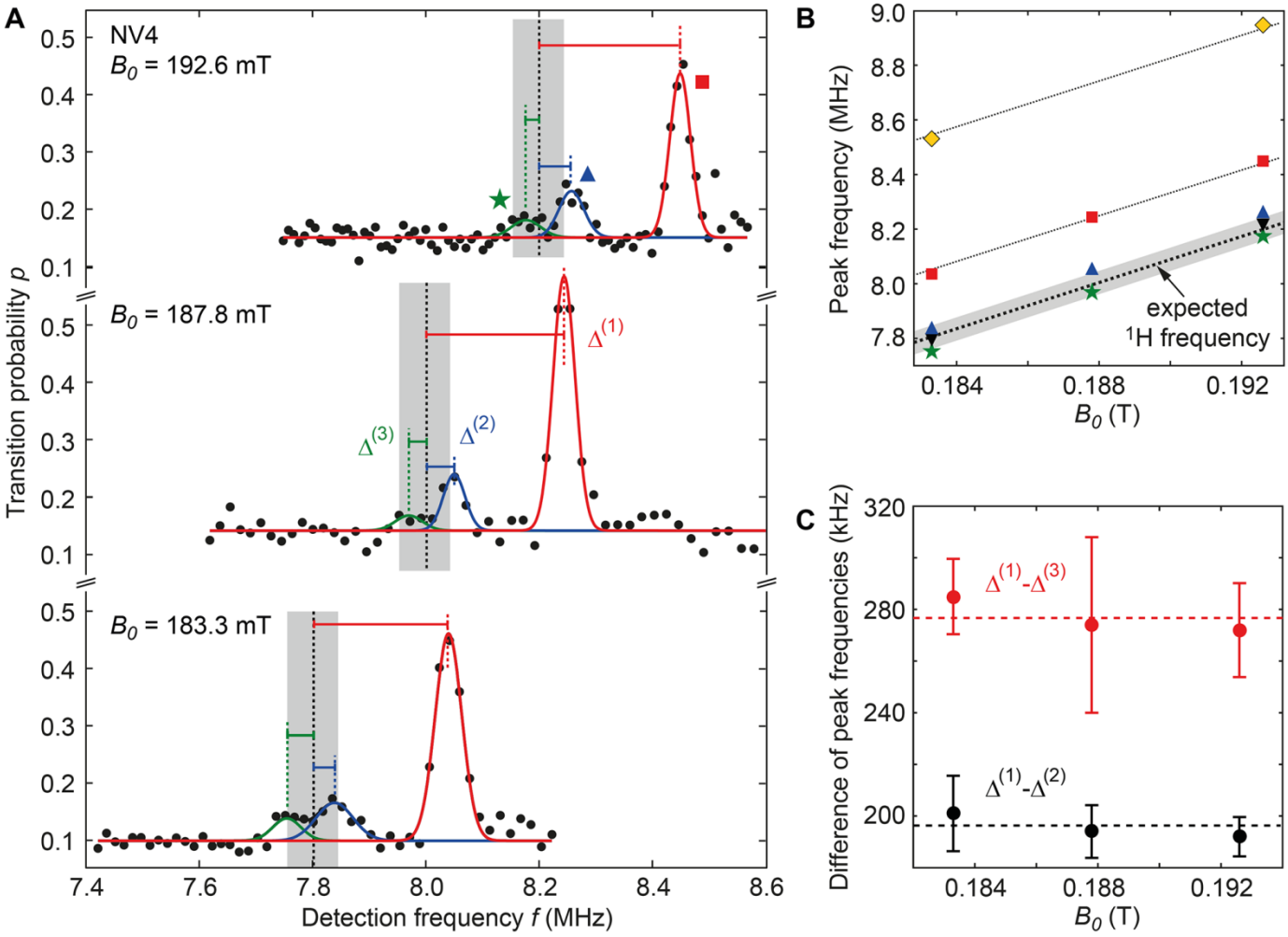

Fig. 2. Zeeman effect and hyperfine coupling of proton spins. (**A**) NMR spectrum (NV4) at three different external fields B_0. All peaks shifted with B_0. In comparison to Fig. 1, two resonances were resolved for the central peak. $\Delta^{(1-3)}$ label the frequency shifts with respect to the expected proton frequency (dashed vertical line). (**B**) Peak frequency as a function of B_0. Yellow diamonds and black triangles show the two peaks from NV5. Diagonal lines have slope $\gamma_n/2\pi$ = 42.6 MHz/T. (**C**) Frequency difference between peaks (1-2) and (1-3), respectively. No dependence on B_0 is seen, as expected for a dipolar hyperfine interaction. Horizontal dashed lines are average values. Error bars are fit error of peak position in 95% confidence.

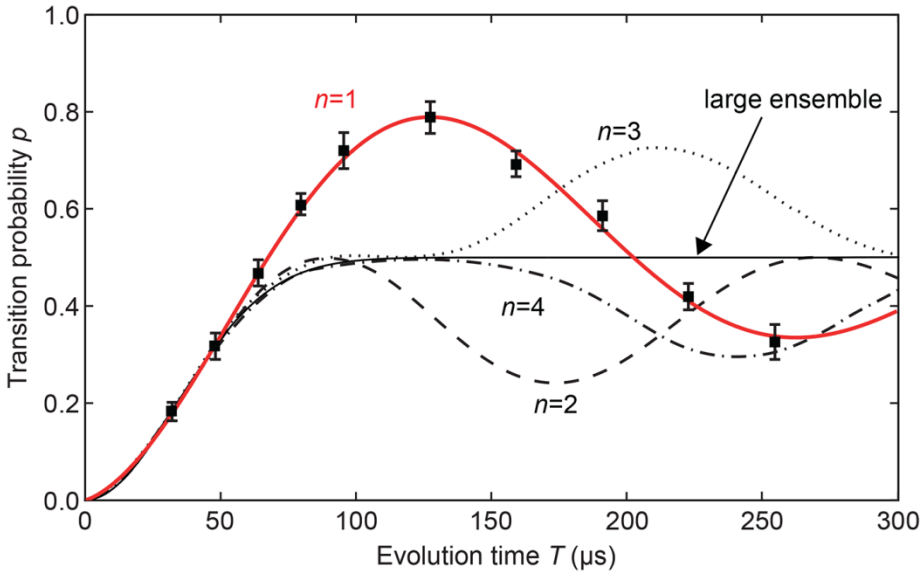

Fig. 3. Coherent joint rotation of the coupled electron-proton two-spin system. Shown is the transition probability for peak (black triangle, NV4) as a function of evolution time T. Bold solid curve shows quantum-mechanical evolution based on a density operator calculation. Other curves are given for comparison and show evolution for an NV center coupled to n = 2, 3, or 4 protons, as well as decoherence due to a "classical" proton spin bath. The oscillation was damped on a time scale of 193 ± 23 μs, which is consistent with the NV spin coherence time of T_2 = 206 ± 8 μs obtained by a separate measurement. Similar curves for NV3 and NV5 are provided in fig. S5.

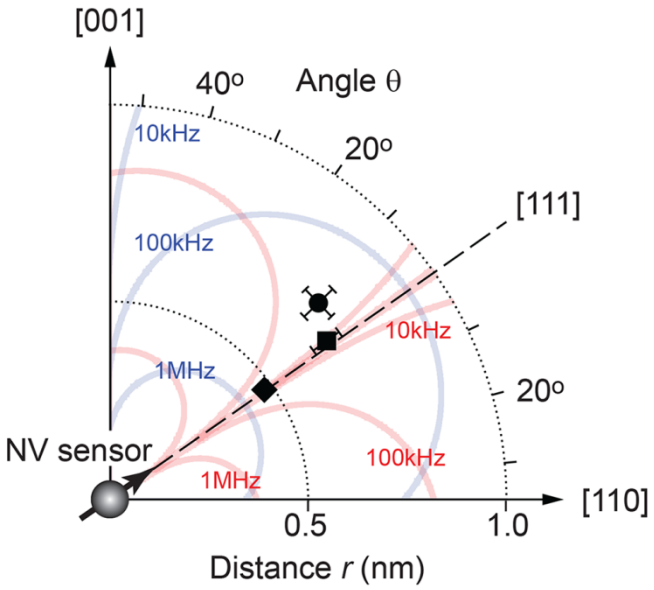

Fig. 4. Two-dimensional spatial mapping of hydrogen nuclei. Three data points are included that showed quantum coherent coupling. (Not enough spectra were measured for other peaks that likely represent more distant protons). Shown are the distance *r* and polar angle θ with respect to a central NV center; equivalent positions at −*r* and around [111] are omitted for clarity. Blue and red contours show isolines for peak shift and coupling frequency, respectively. Error bar reflects fit error or calibration uncertainty in the external magnetic field (±1 mT, ±1°), whichever is larger, and is omitted if smaller than the symbol.

Supplementary Materials for

Single proton spin detection by diamond magnetometry

M. Loretz, T. Rosskopf, J. M. Boss, S. Pezzagna, J. Meijer, and C. L. Degen*

* To whom correspondence should be addressed. E-mail: degenc@ethz.ch

This PDF file includes:

Materials and Methods

Diamond chip engineering

The diamond chip used in this study is the same as the one discussed in Ref. (*6*). The diamond chip was a standard "electronic grade" single crystal with approximate dimensions of $2 \times 2 \times 0.5\,\mathrm{mm}^3$ (ElementSix). The crystal had a (001) surface orientation and was received scaife polished by the manufacturer. The surface was briefly etched by ArCl plasma to remove a few hundred nanometers of material due to possible polishing damage. NV centers were formed by implantation with $^{15}N^+$ ions using an energy of 5 keV and a fluence of 10^{11} cm^{-2} and by subsequent annealing at 850°C in high vacuum ($p < 2 \times 10^{-7}$ millibars) for 2 h. These implantation parameters should lead to NV centers with an average depth of 8 nm and a straggling of ± 3 nm according to stopping-range-of-ions-in-matter calculations (*22*). The diamond was subsequently heated to ∼650°C in ambient air to slowly remove about 10 nm of material by oxidation (*6*). Before deposition of a proton-containing sample, the diamond was cleaned in an acid bath and by heating it in air to 450°C. Surface analysis by atomic force microscopy revealed that air oxidation introduced a slight topography to the surface; as shown in Fig. S1, the surface roughness increased from 0.12 nm-rms before air oxidation to 1.05 nm-rms after air oxidation.

NH_4PF_6 application and proton formation

NH_4PF_6 deposition

The inorganic salt ammonium hexafluorophosphate NH_4PF_6 (99.99 % trace metals basis, Sigma Aldrich) was used as the proton-containing sample. The salt was compressed to a dense pellet of 5 mm diameter and thermally evaporated out of a molybdenum boat. Thermal evaporation was performed at a pressure of 10^{-5} millibars. The NH_4PF_6 film had a nominal thickness of 20 nm based on the quartz crystal reading of the evaporator. Inspection by optical microscopy showed that the film was discontinuous with patches of the surface uncovered by the salt. Moreover, there were indications that the film became less thick and vanished during the experiments. This can be expected from the volatile and hygroscopic nature of the salt. In particular for the NV center where a ^{19}F signal was observed (NV4), the peak reduced with time and the signal eventually disappeared entirely.

Surface characterization

Evidence of a chemical interaction of NH_4PF_6 (and later of KPF_6) with the diamond surface was observed. Although most NV centers were still present after the deposition, some bleached during investigation and NV centers were generally less stable with decreased ODMR contrast and shorter T_2. (No background fluorescence was seen from NH_4PF_6). Depth calibration of one NV center before and after NH_4PF_6 application by NV-NMR showed a reduction of the nominal depth from 5.2 to 2.6 nm, and an associated reduction by a factor of two in the spin coherence time T_2 (see Fig. S3). At the end of the study, the NH_4PF_6 film was removed and replaced with a ~ 150 nm thick thermally evaporated layer of (proton-free) KPF_6. All previously investigated NV centers disappeared after KPF_6 deposition and only very few implanted NV centers were found remaining. Although we do not know the precise chemical reaction, we believe that the interaction of NH_4^+ and PF_6^- ions (or their products) with the top diamond layer, combined with the atomic-scale surface topography introduced earlier, was essential for the formation of the isolated protons observed here.

Proton location

Given the isolated nature of detected single protons we have speculated whether the spins are located on the chip surface or whether they have been incorporated into the crystalline lattice of diamond. Since the diamond surface typically has a significant interface region (∼nm), consisting of varying hybridization (sp^2, sp^3) of carbon atoms, varying surface groups, dangling bonds, adsorbate molecules, and atomic-scale topography, it is difficult to give a precise definition of the surface. Because the distinguishing feature of our protons is their isolated nature (no other hydrogen nuclei right nearby), we have focused our attention on possible

mechanisms that could generate such isolated protons. These are briefly summarized below:

- Isolated protons were formed in pockets of the surface topography during NH_4PF_6 deposition. The chemical reaction with NH_4PF_6 created or enhanced pockets in the surface that were subsequently saturated by hydrogen. The protons are located at the bottom of the interface region. We believe that this is the most likely scenario.

- Protons were formed sub-surface (in the sp^2 or sp^3 region) through impinging NH_4^+ ions. This scenario is unlikely since the kinetic energy of ions was far too low and likely insufficient to even penetrate the adsorbate layer.

- Protons were generated by a chemical reaction and subsequent diffusion into the sp^2 or sp^3 region. A possible chemical reaction could be the decomposition of PF_6^- by H_2O into H^+, F^- and PF_5OH or other reactants. This scenario is unlikely, because H^+ would immediately become hydrated to form H_3O^+. We are further unaware of literature that would describe proton diffusion in crystalline diamond at room temperature.

Experimental setup

The experimental apparatus was a home-built confocal microscope that operated under ambient conditions. Continuous-wave green laser light (CNI 532nm DPSS Laser, 200 mW) was passed through an acousto-optic modulator (Crystal Technology 3200-146, $\sim$ 50 ns rise time) in a double-pass arrangement, and spatially filtered using a single mode optical fiber (Thorlabs). The light was focused onto the diamond surface using a pair of scanning mirrors (Cambridge Technologies) and a high-NA air objective (Olympus UPLSAPO40X2, NA=0.95, 40$\times$). A glass slide with a lithographically patterned Au microwave transmission line was inserted between the objective lens and the diamond chip. Red light emitted by the NV center was collected by the same objective and scanning mirrors, branched off by a dichroic mirror (Omega Optical), and band-pass filtered in the 630-800 nm wavelength range. A free-space single photon counter module (Perkin Elmer SPCM-AQRH-16) was used as the photodetector. A counter card (National Instruments, PCI-6602) was used to time-tag photon counts. Gating and binning of photons was carried out in software.

The microwave pulses were generated by an arbitrary waveform generator (Tektronix, AWG5002C, 600 MS/s) at a carrier frequency of 100 MHz and upconverted to the desired 2-3 GHz using an I/Q mixer (Marki Microwaves, IQ-1545) and a low-phase-noise synthesizer (Phasematrix, Quicksyn FSW-0020). Amplitude and phase modulation was done in software during numerical synthesis of the arbitrary waveform. The microwave signal was amplified by a linear power amplier (HD Communications, HD28271, 30 W) and delivered by passing current through the microwave transmission line in close proximity ($< 10\ \mu\mathrm{m}$) to the sample. Microwaves were terminated in a high-power $50\ \Omega$ load. The Rabi frequencies of pulses were typically around 30 MHz.

Static magnetic fields were applied by means of a NdFeB permanent magnet (KJ Magnetics, N52, 1/2" diameter $\times$ 1" length). Field magnitude and orientation were adjusted by mechanically moving the magnet using an automated translation stage. The magnetic field was aligned with the NV symmetry axis and its magnitude calibrated using optically detected magnetic resonance (ODMR) measurements of the NV center with different magnet positions. All investigated NV centers had the same crystallographic orientation. The uncertainty in the absolute magnetic field and the misaligment from the NV axis were not measured, but from experience we know that they are less than $\pm 1\,\mathrm{mT}$ and $\pm 1^\circ$, respectively. Where the calibration uncertainty was important, reported errors assumed an uncertainty of $\pm 1\,\mathrm{mT}$ and $\pm 1^\circ$, respectively. The typical fields used in our experiments were between 170-200 mT.

Signal detection protocol

NMR signals were measured using a Carr-Purcell-type decoupling sequence, similar to previous NV-NMR experiments (*5,6*). A pulse timing diagram is shown in Fig. S2. A laser pulse ($\sim 2\ \mu\mathrm{s}$) was used to pump

the NV center into the $m_S = 0$ spin state. Next, a $\pi/2$ microwave pulse resonant with the $m_S = 0$ to $m_S = -1$ transition generated a coherent superposition of the two spin states. A series of evenly spaced π pulses were used for dynamical decoupling. The phases of pulses were varied according to the XY8 protocol (*23*) as indicated in Fig. S2, and cosine-square pulse shaping was used. At the end of the decoupling sequence, a second $\pi/2$ pulse was applied to convert the coherence back into detectable polarization. Since the fluorescence of the NV center is reduced by about 30% when in $m_S = -1$ compared to $m_S = 0$, a second laser pulse (~ 2 μs) can be used to probe the final spin state.

Reported in all our experiments is the transition probability p, which is the probability that the spin is found in state $m_S = -1$ at the end of the sequence. We have measured p by simultaneously recording two references, ref_0 and ref_{-1} (see Fig. S2), which give the fluorescence intensity in the $m_S = 0$ and $m_S = -1$ spin states. The transition probability is then given by $p = (\mathrm{ref}_0 - \mathrm{sig})/(\mathrm{ref}_0 - \mathrm{ref}_{-1})$, where "sig" is the fluorescence intensity of the signal. The pump-probe sequence shown in Fig. S2 was typically repeated a few million times until sig, ref_0 and ref_{-1} had integrated photon counts of $> 10^4$.

Estimation of nuclear magnetic field

The transition probability depends on the phase $\Delta\phi$ picked up during coherent evolution under the influence of a (fluctuating) magnetic field,

$$p = \sin^2\left[\frac{1}{2}\Delta\phi\right] \tag{1}$$

where the phase

$$\Delta\phi = \int_0^T dt\gamma_e B_z(t) Y(t) \tag{2}$$

is a convolution of the modulation function $Y(t)$ with the magnetic field $B_z(t)$, and T is the duration of coherent evolution. The modulation function, plotted in Fig. S2, is simply given by the periodic spin flips as $Y(t) = (-1)^{[t/\tau]}$, where τ is the interpulse delay. The Fourier transform of $Y(t)$ determines the associated "filter function" $\tilde{Y}(f)$, also plotted in Fig. S2. The filter function acts as a narrow band filter that passes signals at the center frequencies $f = k/(2\tau)$, with $k = 1, 3, 5, ...$, and that has a filter bandwidth of $\Delta f = 1/T$. For our experiments, we have always used the fundamental pass band $k = 1$ where $f = 1/(2\tau)$. We have verified by scanning a wide range of f that detected signals indeed belonged to $k = 1$, and not to a higher order k.

Classical signals

NMR signals detected in reported experiments showed two different transition probability functions $p(T)$, which we denote as "classical" and "quantum" signals. Large ensembles of nuclear spins produce a classical response owing to the classical magnetic noise generated by spin noise. This noise has random phase and magnitude, and the magnitude has a Gaussian distribution. At resonance (that is, if f equals the nuclear Larmor frequency), the transition probability is

$$p_{\mathrm{ensemble}}(T) = \frac{1}{2} - \frac{1}{2}\exp\left[-\frac{1}{2}T^2\gamma_e^2 B_{\mathrm{rms}}^2\right], \tag{3}$$

where B_{rms} is the rms magnetic field (component along NV axis) produced by the nuclear spin precession at the location of the NV center. Importantly, for classical decoherence, the transition probability will always be $p(T) \leq 0.5$.

Quantum signals

A different evolution of $p(T)$ is seen for quantum coherent coupling to single proton spins. As discussed in the Supplementary Text as well as in Refs. (*15,17*), the transition probability for an NV center at resonance is

$$p_{\mathrm{single\ proton}}(T) = \frac{1}{2} - \frac{1}{2}\cos(a_\perp T/\pi), \tag{4}$$

where $a_\perp$ is the transverse component of the hyperfine coupling. Simultaneously, the resonance frequency is shifted from the "bare" Larmor frequency $\gamma_n B_0$ by $a_{||}/2$, where $a_{||}$ is the parallel component of the hyperfine coupling. Here we assume that the interaction is dipolar, and that the external bias field is much stronger than the hyperfine interaction.

Correction for finite pulse lengths

Because the interpulse delay τ becomes very short at high detection frequencies, π pulses consume a significant fraction of the free evolution time. The phase pickup described by Eq. (2) becomes less efficient, and B_{rms} and $a_\perp$ values are underestimated. Reported B_{rms} and $a_\perp$ values have therefore been corrected to account for the less efficient phase accumulation.

Using a density operator simulation we have determined that phase pick-up during τ is slowed down by a factor $x = 1-0.5t_\pi/\tau$ for square-shaped π-pulses, and by a factor $x = 1-0.25t_\pi/\tau$ for cosine-square-shaped π-pulses (with equal peak amplitude), where t_π is pulse duration. Using values typical for our experiments, $\tau = 60\,\mathrm{ns}$, $t_\pi = 40\,\mathrm{ns}$ and cosine-square pulse shaping, the factor is $x = 0.83$. Reported values for B_{rms} and $a_\perp$ are the fit values by Eq. (3) and Eq. (4), divided by x.

Estimation of proton positions

From the two components of the hyperfine interaction $a_{||}$ and $a_\perp$, the distance r and internuclear angle θ between the NV center and the proton can be determined:

$$a_{||} = \frac{\mu_0\gamma_e\gamma_n\hbar}{4\pi r^3}(3\cos^2\theta - 1), \tag{5}$$

$$a_\perp = \frac{\mu_0\gamma_e\gamma_n\hbar}{4\pi r^3}3\cos\theta\sin\theta. \tag{6}$$

We again assume that the interaction is dipolar, and that the external bias field is much stronger than the hyperfine interaction. $a_{||}$ and $a_\perp$ have units of angular frequency. The angle θ and position r as a function of $a_{||}$ and $a_\perp$ are:

$$\theta = \arctan\left\{\frac{1}{2}\left(-3\frac{a_{||}}{a_\perp} + \sqrt{9\frac{a_{||}^2}{a_\perp^2}+8}\right)\right\}, \tag{7}$$

$$r = \left\{\frac{\mu_0\gamma_e\gamma_n\hbar(3\cos^2\theta-1)}{4\pi a_{||}}\right\}^{1/3}. \tag{8}$$

Supplementary Text

Simulation of quantum evolution

Hamiltonian

Density operator simulations were performed to calculate the quantum evolution of the transition probability $p(T)$ for different multi-spin systems. Simulations were all performed in a rotating frame resonant with the $m_S = 0$ to $m_S = -1$ transition. The Hamiltonian considered was (in units of angular frequency):

$$\hat{H} = \sum_{i=1}^{n}\gamma_n B_0\hat{I}_{z,i} - \hat{\vec{S}}\sum_{i=1}^{n}A_i\hat{\vec{I}}_i + \sum_{\substack{i,j=1\\ j>i}}^{n}\omega_{D,ij}\hat{I}_{z,i}\hat{I}_{z,j} \tag{9}$$

where $\hat{\vec{S}} = (\hat{S}_x, \hat{S}_y, \hat{S}_z)$ are the operators of the NV electronic spin, $\hat{\vec{I}}_i = (\hat{I}_{x,i}, \hat{I}_{y,i}, \hat{I}_{z,i})$ are the operators of the nuclear spins, $1 \le i, j, \le n$ are the indices for the nuclear spins, and n is the number of nuclear spins. The first term is the nuclear Zeeman interaction, the second term is the hyperfine interaction with coupling

tensors A_i, and the third term is the nuclear-nuclear dipole coupling with coupling constants $\omega_{D,ij}$. For this analysis the coupling to ^{15}N or ^{13}C nuclei or a detuning of the microwave frequency was neglected. We have verified in separate simulations that those do not affect relevant spin dynamics. Relaxation was neglected for the simulation, but was considered as a phenomenological decay once the transition probability $p(T)$ had been calculated.

Simulations further took advantage of the fact that in our experiments, nuclear Zeeman frequencies are much larger than the hyperfine interaction ($\gamma_n B_0 \gg ||A_i||$), so that the hyperfine interaction can be separated into secular and nonsecular contributions,

$$\sum_{i=1}^{n} \hat{\vec{S}} A_i \hat{\vec{I}}_i \approx \sum_{i=1}^{n} \hat{S}_z (a_{||,i} \hat{I}_{z,i} + a_{\perp,i} \hat{I}_{x,i}). \tag{10}$$

Here $a_{||,i}$ and $a_{\perp,i}$ are the parallel and transverse components of the hyperfine coupling (see main text), respectively. (An appropriate rotation of the coordinate system was used such that $a_\perp$ is along x). Since we focused on the $m_S = 0$ to $m_S = -1$ transition, the Hamiltonian can be separated into the electronic and nuclear subspaces. The Hamiltonian in the nuclear subspace then takes on one of two forms, depending on whether the electronic spin is in the $m_S = 0$ or the $m_S = -1$ state, respectively,

$$\hat{h}_0 = \sum_{i=1}^{n} \gamma_n B_0 \hat{I}_{z,i} + \sum_{\substack{i,j=1 \\ j>i}}^{N} \omega_{D,ij} \hat{I}_{z,i} \hat{I}_{z,j} \tag{11}$$

$$\hat{h}_{-1} = \sum_{i=1}^{N} \gamma_n B_0 \hat{I}_{z,i} + \sum_{i=1}^{N} (a_{||,i} \hat{I}_{z,i} + a_{\perp,i} \hat{I}_{x,i}) + \sum_{\substack{i,j=1 \\ j>i}}^{N} \omega_{D,ij} \hat{I}_{z,i} \hat{I}_{z,j} \tag{12}$$

(We have used lower case $\hat{h}$ to distinguish the nuclear-spin-only Hamiltonian from the full Hamiltonian).

Transition probability

The transition probability p is given by

$$p = \mathrm{Tr}\left[\langle -1|\hat{U}_{-\pi/2} \hat{U}_{\mathrm{CP}} \hat{U}_{\pi/2} \left(|0\rangle\langle 0| \otimes \hat{\rho}_{\mathrm{nuc}}\right) \hat{U}^\dagger_{\pi/2} \hat{U}^\dagger_{\mathrm{CP}} \hat{U}^\dagger_{-\pi/2} |-1\rangle\right] \tag{13}$$

where $|0\rangle$ is the $m_S = 0$ state and $|-1\rangle$ is the $m_S = -1$ state, and $\hat{\rho}_{\mathrm{nuc}}$ is the density matrix of nuclear spins. $\hat{U}_{\pm\pi/2}$ denotes the initial and final $\pi/2$ pulse required to create the coherent superposition between $|0\rangle$ and $|-1\rangle$ and convert it back to detectable polarization. $\hat{U}_{\mathrm{CP}}$ is the propagator of the XY8 detection sequence which consists of N spin echoes formed by a π rotation sandwiched between two $\tau/2$ free evolution periods,

$$\hat{U}_{\mathrm{CP}} = \left(\hat{U}_{\text{spin echo}}\right)^N, \tag{14}$$

$$\hat{U}_{\text{spin echo}} = \hat{U}\left(\frac{\tau}{2}\right) \left(|0\rangle\langle -1| + |-1\rangle\langle 0|\right) \hat{U}\left(\frac{\tau}{2}\right). \tag{15}$$

The basic building block of nuclear propagation,

$$\hat{U}\left(\frac{\tau}{2}\right) = |0\rangle\langle 0|\hat{u}_0 + |-1\rangle\langle -1|\hat{u}_{-1} \tag{16}$$

can be expressed using the two subspaces with the propagators

$$\hat{u}_0 = e^{-i\tau \hat{h}_0/2}, \tag{17}$$

$$\hat{u}_{-1} = e^{-i\tau \hat{h}_{-1}/2}, \tag{18}$$

where we have again used lower cases to emphasize that these are nuclear-spin-only operators. Combining equations, the transition probability $p(T)$ becomes

$$p = \frac{1}{2} - \frac{1}{2}\mathrm{Re}\left(\mathrm{Tr}\left[\hat{\rho}_{nuc}\left(\hat{u}^\dagger_{-1}\hat{u}^\dagger_0\hat{u}^\dagger_0\hat{u}^\dagger_{-1}\right)^{N/2}\left(\hat{u}_0\hat{u}_{-1}\hat{u}_{-1}\hat{u}_0\right)^{N/2}\right]\right), \tag{19}$$

where the evolution time T is set by the number of π rotations N as $T = N\tau$.

Performed simulations

Several scenarios were considered. For the simulations shown in Fig. 3, the dipolar coupling between nuclei was neglected ($\omega_{D,i,j} = 0$ for all i, j) and nuclear spins were assumed to have the same hyperfine coupling parameters ($a_{||,i} = a_{||}$ and $a_{\perp,i} = a_{\perp}$ for all i). This scenario would be relevant for nuclear spin clusters with rapid internal motion, such as rotating CH_3 or NH_4 groups. We have also calculated $p(T)$ trajectories for other Hamiltonians that include inequivalent $a_{||,i}$ and $a_{\perp,i}$ as well as non-zero $\omega_{D,i,j}$. These Hamiltonians would all produce multiple peaks in the NMR spectrum and/or multifrequency oscillations of $p(T)$.

For Fig. 3, $a_{||}$ and $a_{\perp}$ were chosen such that curves would fit the initial rise of $p(T)$ in the first approx. 50 μs. A phenomenological exponential decay $\propto e^{-T/T_2}$ was superimposed on all plotted $p(T)$ curves to account for relaxation.

Control experiments

Other diamond substrates and other samples

^{1}H signals were measured on over 20 NV centers and on four different single crystal diamond substrates and three different surface coatings. Tested substrates included a δ-doped ^{12}C epilayer, the present $^{\mathrm{nat}}$C substrate (after oxygen etching), a second $^{\mathrm{nat}}$C substrate (after oxygen etching), and an as-grown ^{12}C substrate. NV centers in the latter three substrates were created by ion implantation. All surfaces were oxygen terminated. Tested surface coatings with measurable ^{1}H signals included microscope immersion oil, NH_4PF_6, and naturally present adsorbate molecules ("no coating"). We observed that only NH_4PF_6 would show isolated proton peaks. We have not attempted to test a second NH_4PF_6-coated substrate due to the degrading effect of NH_4PF_6 to the delicate diamond chip surface.

One NV center of the present study (NV3) was measured before and after NH_4PF_6 deposition. Before deposition (and with immersion oil applied to the surface), the NV center showed a resonance at the expected ^{1}H frequency with a defect depth of 5.2$\pm$0.5 nm. After NH_4PF_6 deposition, the same NV center shows two resonances (see Fig. 1D) with a defect depth of 2.6$\pm$0.4 nm. Moreover, the coherence time T_2 was reduced from 26 μs to 11 μs (see Fig. S3).

As a further control, we have attempted to remove the single protons by replacing NH_4PF_6 with proton-free KPF_6, but found this procedure to eliminate all investigated near-surface NV centers in the substrate (see Materials and Methods).

Imperfections in the detection sequence

A number of tests were performed to verify that the observed NMR signals were due to protons and not due to imperfections in the microwave pulse sequence. In particular, we have recorded ^{1}H NMR signals using different π pulse amplitudes and durations and using different sampling frequencies and carrier frequencies for microwave generation. We have also measured ^{1}H signals on two different experimental setups, with different RF hardware, and found no discrepancies. A large window of NMR frequencies was further scanned to verify that observed peaks corresponded to the fundamental frequency of the filter function.

Possible couplings to ^{13}C and ^{15}N nuclei

Additional hyperfine couplings to the ^{15}N nucleus of the NV center and nearby lattice ^{13}C nuclei were occasionally observed as additional peaks in the NV-NMR spectrum. These peaks behave distinctly different from the ^{1}H resonances, and most importantly, do not follow the $\gamma_n = 42.6\,\mathrm{MHz/T}$ scaling with magnetic field B_0. ^{13}C resonances were always present at low NMR frequencies ($\sim$ 2 MHz). ^{15}N resonances were occasionally seen at low frequencies ($<$ 3 MHz) when the magnetic field was not properly aligned with the NV symmetry axis.

Measuring the hyperfine interaction on the NV spin resonance

The question arose whether the hyperfine interaction between the NV spin and the nuclear spin in the order of several hundreds of kHz could also be observed on the resonance of the NV spin. In Fig. S4 the optical

detected magnetic resonance (ODMR) measurements for NV3 to NV5 are shown. The resonance line is split by $\sim$3 MHz due to the ^{15}N hyperfine interaction and the residual linewidths for all three NV centers are rather large, of order 1 MHz, which makes it difficult to resolve the hyperfine interactions on the NV center resonance.

Detection of free nuclear precession

As a further test, we have attempted to detect the free nuclear precession (*36*) of protons by using two XY8-N sequences spaced by a variable delay time t, and looking for oscillations in the detected signal as a function of t. No oscillation was observed within experimental error. We attribute this to the poor efficiency of the sequence (with very short pulse delays), or to inhomogeneous broadening of the proton resonance.

Detection sensitivity

We have estimated the minimum detectable magnetic field using Eq. (22) provided with the Supplementary Material of Ref. (*39*):

$$B_{\min} = \left[\frac{1}{4} e^{-\frac{T}{T_2}} \epsilon \gamma_e^2 T^{1.5} (T_{\rm tot} R)^{0.5}\right]^{-0.5}. \tag{20}$$

Here, T is the evolution time, T_2 is the decoherence time under CP decoupling, ϵ is the optical contrast between $m_S = 0$ and $m_S = -1$ states, $\gamma_e = 2\pi \times 28\,\mathrm{GHz}$ is the electron gyromagnetic ratio, $T_{\rm tot}$ is the total time of the experiment, and R is the photon collection efficiency given as number of photons per probe laser pulse.

Current experiment

Taking the experimental parameters for NV4, $T_2 = 200\ \mu$s, $\epsilon = 0.25$, $R = 0.015$, and setting $T = T_2$ and $T_{\rm tot} = 60\,$s, one obtains $B_{\min} = 23\,$nT. This can be converted into a minimum detectable hyperfine coupling $a_\perp \approx \gamma_e B_{\min} = 640\,$Hz. Comparing this to the magnitude of $a_\perp$ at a certain distance r, one finds that $r_{\max} \approx 4\,$nm. Thus, the coupling of a single proton in 4 nm distance could be detected with unit SNR using one minute of averaging. This distance is approximate, since $a_\perp$ also depends on the angle θ.

Estimated future improvements

Improvements in photon collection efficiency will directly improve the magnetic field sensitivity. Using nanopillar waveguides, photon count rates as high as 1.5 MC/s have been reported [S. A. Momenzadeh et al., arXiv:1409.0027], which is about 30$\times$ higher than the count rate for our experiment. Repetitive readout via nuclear quantum storage (Ref. (*35*)) has shown a 10$\times$ improvement in readout efficiency. If combined, the two advances would yield a 300$\times$ improvement in the photon collection efficiency R, or equivalently, a 17$\times$ improvement in $B_{\min}$. The coupling of a single proton could then be detected at a distance of 10 nm.

Supplementary Figures

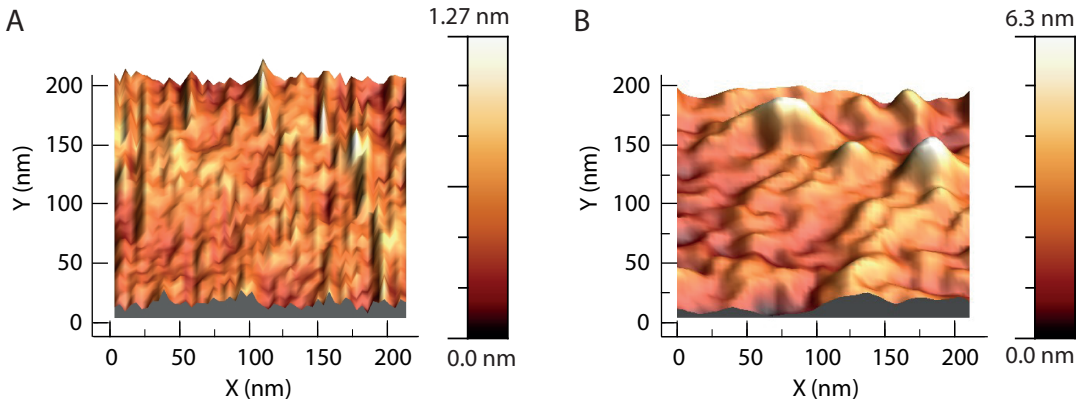

Figure S1: Representative atomic force microscope (AFM) images of the diamond subtrate (A) after ArCl etching and before oxygen etching, and (B) after oxygen etching in air at 650°. Surface roughness is 0.12 nm-rms in (A) and 1.05 nm-rms in (B), respectively.

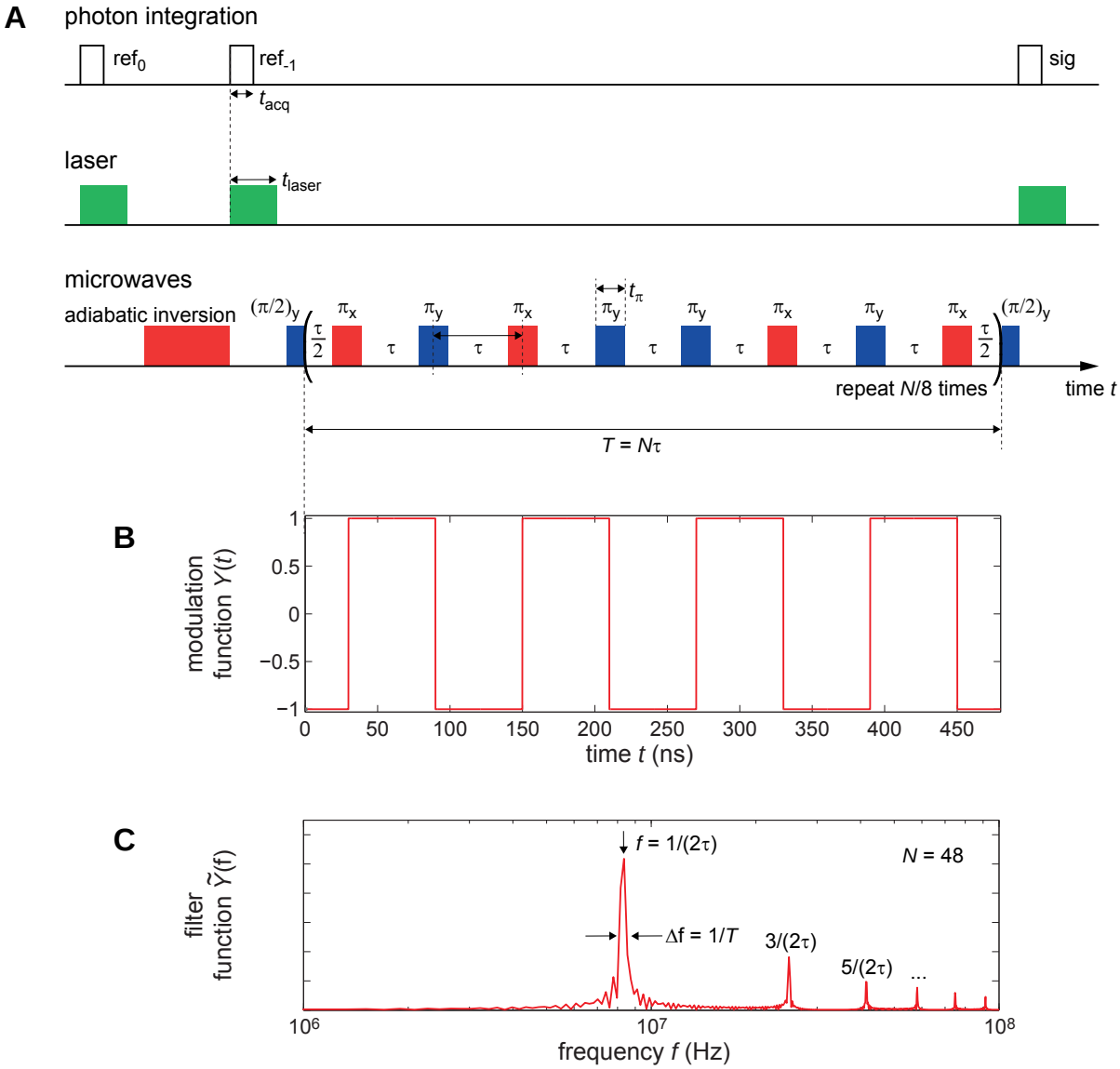

Figure S2: Details of the detection protocol. (A) Pulse-timing diagram of laser pulses, microwave pulses, and photon detection. Times indicate delays and pulse lengths. $\pi/2$ and π denote spin rotations by microwave pulses. x an y indicate pulse phases that were according to the XY8 sequence. (B) Modulation function $Y(t)$ of the sequence, shown for a delay time of $\tau = 60$ ns. (C) Filter function $\tilde{Y}(f)$ associated with $Y(t)$. Example filter function is shown for a sequence consisting of $N = 48$ pulses (a few hundred pulses were used in typical experiments). The fundamental filter frequency for the chosen delay time is $f = 1/(2\tau) = 8.33$ MHz and the filter bandwidth is $\Delta f = 1/T = 1/(N\tau) = 0.35$ MHz.

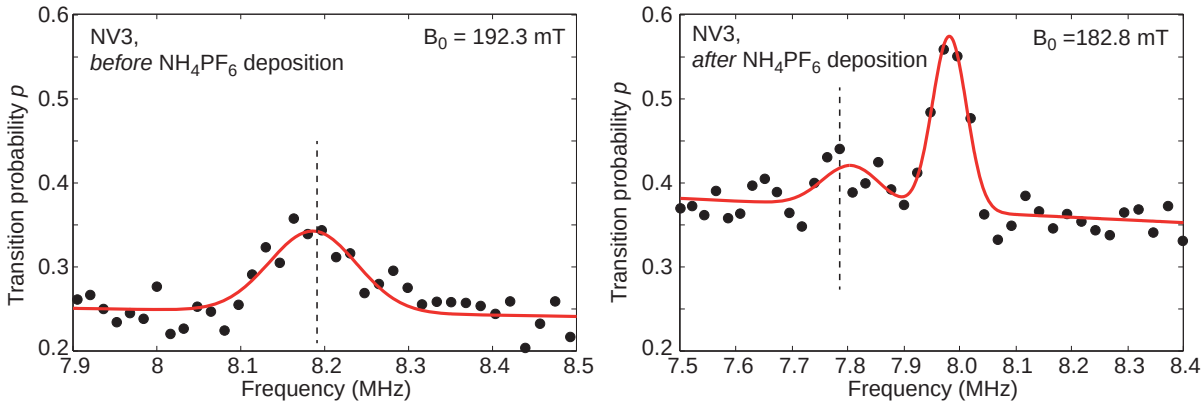

Figure S3: Proton NMR spectra of NV3 before and after application of NH_4PF_6 . Before NH_4PF_6 deposition, only a single peak is seen at the expected ^{1}H frequency (dashed vertical lines) that originates from an ensemble of more distant protons, such as those in terminating atoms and adsorbate molecules. After NH_4PF_6 application, an additional peak at slightly higher frequency appears due to the generated single proton.

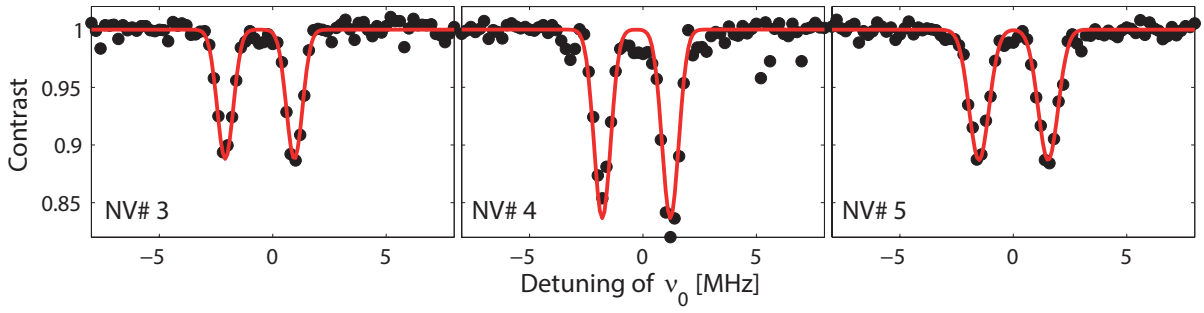

Figure S4: Optically detected magnetic resonance (ODMR) spectra for NV3 to NV5. ODMR spectra were recorded using the method reported by Dreau et al., Phys. Rev. B 84, 195204 (2011).

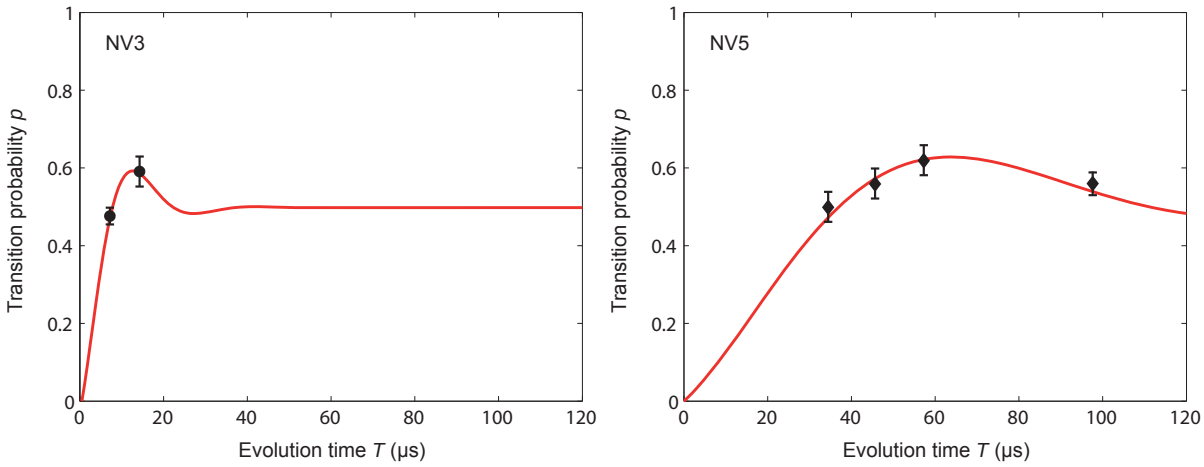

Figure S5: Coherent joint rotation of peaks (●,NV3) and (◆,NV5), similar to Fig. 3. The bold solid lines are fits to Eq. (4) using $a_\perp$ as the free fit parameter and T_2 from table S1 as a fixed parameter.

Supplementary Tables

		Number of pulses N	Evolution time T (μs)	T_2 (μs)	B_0 (mT)	B_{rms} (μT)	Nominal depth d (upper bound) (nm)
Fig. 1C	NV1	512	30.6	97±3	183.6	2.0±0.2	2.2±0.2
	NV2	128	8.2	6.8±0.3	183.3	2.0±0.4	2.2±0.3
	NV3	160	10.3	11±5	182.8	1.2±0.3	3.1±0.7
	NV4	768	49.1	223±10	183.6	-	-
	NV5	768	49.2	106±5	183.3	0.7±0.1	4.4±0.4
Fig. 2A	upper	1280	77.2	206±8	192.6	-	-
	middle	1280	79.2	-	187.8	-	-
	lower	1024	65.0	-	183.3	-	-

Table S1: Experimental and simulation parameters for NMR spectra shown in Figs. 1 and 2. N is the number of π pulses. T is the evolution time at expected ^{1}H frequency. T_2 is the decoherence time under Carr-Purcell decoupling. B_0 is the magnetic field inferred from the NV ODMR frequency. B_{rms} is the rms magnetic field according to Eq. (3). d is a nominal depth of the NV center inferred from B_{rms} according to Ref. (*6*) based on the NH_4PF_6 proton density of $\rho^{(^1\mathrm{H})} = 3.2 \cdot 10^{28}\,\mathrm{m}^{-3}$. This model assumes a flat surface covered by an infinitely thick proton layer. Since our surface had topography (was not flat) and was likely only covered by a thin layer of adsorbate molecules and terminating groups, this nominal depth is overestimated and the NV centers actually lie substantially closer to the surface.

Fig. 2A (NV4)	Expected ^{1}H frequency (MHz)	Peak (1) freq. (MHz)	Peak (2) freq. (MHz)	Peak (3) freq. (MHz)	$\Delta^{(1)}$ (kHz)	$\Delta^{(2)}$ (kHz)	$\Delta^{(3)}$ (kHz)
upper	8.199	8.449±0.003	8.257±0.007	8.177±0.018	250±3	58±7	-22±18
middle	7.995	8.244±0.002	8.050±0.010	7.970±0.034	249±2	55±10	-25±34
lower	7.803	8.036±0.002	7.835±0.014	7.751±0.014	233±4	32±14	-52±14

Table S2: Summary of peak shifts used for Fig. 2. Expected ^{1}H frequency is $\gamma_n B_0$ from Table S1. Peak (1-3) frequencies are the respective peak frequency determined by a Gaussian fit. $\Delta^{(i)}$ represents the difference between the expected ^{1}H frequency and frequency of peak i. The frequency difference equals half the parallel hyperfine coupling parameter $a_{||}^{(i)}$. Errors indicate 95% confidence interval from the fit, but do not include the global ± 1 mT (± 42.6 kHz) calibration uncertainty in B_0.

Fig. 4	Peak	Expected ^{1}H frequency (MHz)	Peak frequency (MHz)	$a_{\|\|}/2\pi$ (kHz)	$a_\perp/2\pi$ (kHz)	Distance r (nm)	Polar angle θ (°)
NV3	(●)	7.782	7.975±0.006	386±12	85±35	0.74±0.06	8.3±3.8
NV4	(■)	8.199	8.449±0.003	500±6	14.5±0.3	0.68±0.04	1.1±0.2
NV5	(◆)	7.803	8.531±0.003	1456±6	20±4	0.48±0.01	0.5±0.1

Table S3: Summary of parameters for single protons used for Fig. 4. Symbols represent peaks marked in Fig. 1C and 2A. Expected ^{1}H frequency is $\gamma_n B_0$ from Table S1. Peak frequency is center frequency of the single ^{1}H peak determined by a Gaussian fit. $a_{||}$ is the parallel component of the hyperfine interaction, given by twice the difference between expected ^{1}H frequency and peak frequency. $a_\perp$ is the vertical component of the hyperfine interaction, which was derived from on Fig. 3 for NV4 and on Fig. S5 for NV3 and NV5 using Eq. (4). Distance and polar angle are according to the relation between $a_{||}$, $a_\perp$, r and θ given in the Materials and Methods section. Frequency errors indicate 95% confidence interval from fits. Errors in r represent uncertainty in absolute field calibration ($\pm 1\,\mathrm{mT}$, equivalent to $\pm 2 \cdot 42.6\,\mathrm{kHz}$ in $a_{||}$) rather than the (smaller) fit errors. Errors in θ represent propagated fit errors; here the absolute uncertainty is $\pm 1°$. Error bars in Fig. 4 denote the fit error or calibration uncertainty, whichever is larger.